Smoothed Particle Hydrodynamics for investigating hydraulic and mechanical behaviour of an embankment under action of flooding and overburden loads

M. Gholami Korzani[a], S. A. Galindo-Torres[a,b], A. Scheuermann[a], D. J. Williams[a]

[a]*School of Civil Engineering, The University of Queensland, St Lucia (Brisbane) QLD 4072, Australia*
[b]*School of Mathematics and Physics, The University of Queensland, St Lucia (Brisbane) QLD 4072, Australia*

Abstract

Extreme weather events, such as floods, are becoming more frequent in future with all consequences concerning the safety especially of water retaining structures, in particular, levees used as technical flood protection. The knowledge and correct consideration of coupled hydro-mechanical processes influencing the failure and post-failure behaviour of water saturated soils are of paramount significance for the assessment of hydraulically loaded geotechnical structures. This study focuses on the modelling of the processes governing the behaviour of water saturated soils using Smoothed Particle Hydrodynamics (SPH) on the example of a homogeneous embankment under different loading conditions. This paper aims to improve available SPH framework in order to enhance soil-water interaction in this method for geotechnical engineering investigations. To achieve this goal, the suggested approach is validated intensively by various well-known problems. Finally, the verified tool is used to investigate the hydro-mechanical behaviour of homogeneous embankments under simultaneous hydraulic and mechanical loading. The simulation results prove that the suggested approach is capable of simulating relevant hydraulic and mechanical processes governing the deformation behaviour of hydraulically loaded structures beyond the failure point allowing the detailed analysis of the post-failure behaviour characterised by large deformations.

Keywords: Smoothed particle hydrodynamics (SPH); dry and saturated soil; soil-water interaction; elastic-plastic constitutive model; seepage flow; embankment

1. Introduction

Embankments are important structures in geotechnical engineering. Their application ranges from storing water either permanently as dams or temporarily as levees for flood protection purposes. Moreover, embankments are used for providing the foundation of road and railway infrastructure and are used as a measure to compensate for the unevenness of the terrain. Embankments, in general, are exposed to the atmosphere due to their geometry. As a consequence, precipitation and evaporation can cause large variations in the water content within the embankment. Additionally, embankments can be temporarily hydraulically loaded due to flooding either as levees, since they are built for this purpose, or unintentionally in the case of embankments for infrastructure when a catchment becomes flooded and the culvert is not able to release the water fast enough. Against the background of the more frequently occurring extreme weather conditions caused by climate change, these situations need to be considered seriously in the design of embankments and for the safety analysis of existing structures.

In the case of a flood event, water infiltrates into the embankment creating a phreatic surface which moves transiently through the embankment body towards the downstream slope. The phreatic surface seeps out of the downstream slope at a height approximately one-third of the water level at the upstream side

Email address: m.gholamikorzani@uq.edu.au (M. Gholami Korzani)

slope. Hence, the flow forces created by the water leaving the embankment body can potentially lead to a failure of the downstream side slope. If the embankment is at the same time mechanically loaded, the situation becomes even more severe. In the case of levees, the crest is frequently used as levee defense path for vehicles and persons. During flooding, vehicles are usually not allowed to drive on levees. Persons, however, are needed to for example enlarge the levee height with sand bags, which create an additional static load. Under such extreme loading conditions, levees frequently show severe deformations of the crest and downstream slope without failing either because the water level started to drop or measures have been put in place which stabilised the structure.

This kind of situation is realistic and needs to be considered in the analysis of the safety of existing levees, which requires the consideration of not only the hydraulic and mechanical processes but also their interaction in a way that large deformations can be considered. Several numerical and experimental studies have been conducted on the stability of embankments. In 2013, Larese et al. [28] used a coupled Particle Finite Element Method (PFEM)-Eulerian approach to simulate over-topping of rockfill dams. They used non-Newtonian law (Bingham like rheology) for simulating rockfill material and compared the results with experiments. Zwanenburg et al. [48] in 2012, and Koelewijn and Lottum [25] in 2013 carried out full-scale tests to investigate failure mechanisms of levees under simultaneous hydraulic and mechanical loading from the crest. As a consequence of these tests [25], in 2011 a software package called Virtual Dike [34] was developed based on the Finite Element Method (FEM) with tools for considering pore water pressure to predict failures caused by the considered loading condition.

FEM is the most popular numerical scheme in computational geomechanics. However, large deformations due to situations introduced before are very common in geotechnical engineering always causing numerical problems as mesh distortion needs to be numerically handled. In order to deal with large deformations, mesh-free methods can be usually found more efficient. While the Discrete Element Method (DEM) [14] provides one possible solution, it is suitable for small scaled problems only due to the long computational time. Furthermore, DEM [15] and FEM [27] need to be coupled with a suitable fluid solver scheme for simulating water motion in order to consider soil-water interaction. Recently, a rather new mesh-free method called Smoothed Particle Hydrodynamics (SPH) has been developed and suggested for considering large deformation and investigating post-failure processes in Geomechanics [5–7, 12]. Since this method is continuum based and grid-less, it can be an appropriate solution to simulate soil behaviour in real scale. Furthermore, this method is already well-established in hydrodynamics [16] which provides the opportunity to simulate and couple both phases, soil and water, in one scheme.

Only few studies already use SPH in combination with soil constitutive relationships to simulate problems in geotechnical engineering. Firstly, Bui et al. [6] in 2007 defined soil-water interaction in SPH using effective stress concept ($\sigma' = \sigma - u_w$) and Darcy's Law. In this approach, the total stress is initially calculated, and it will be then reduced by the pore water pressure to obtain the effective stress for calculating material related variable. Simultaneously, the frictional drag force due to water seepage is applied to soil particles. This type of interaction was followed by Grabe and Stefanova [20, 21], Huang et al. [24] and Wang et al. [47] by adding new features including the Forchheimer equation and mixture theory. Although these recent papers are very useful in the case of unsaturated soil simulations because of the mixture theory, the pore water pressure might be over-estimated in these works if the water table is above the ground surface; however, such problems in geotechnical engineering can practically happen. To solve this issue in the available schemes, Bui and Fukagawa [5] in 2013 deployed SPH for investigating the sliding failure in an embankment under hydrostatic pore water pressure condition. In their solution, the authors provide a formulation for considering hydrostatic pore water pressure (no flow) by defining the water level manually for a fully submerged soil sample. While SPH provides a most suitable platform for simulating hydro-mechanical processes, there is still need for improving this method to overcome the issue coming along with the consideration of water flow and dynamic water level changes during simulations.

The aims of this work are to provide an alternative approach in SPH for studying the hydro-mechanical behaviour of earthen structures in geotechnical engineering and present its application to the investigation of an embankment in various flooding situations. The paper is organized as follows: Section 2 describes the SPH formulations briefly; several validations are provided in Section 3; results of the numerical study conducted on the considered problem of a hydraulically and mechanically loaded embankment are presented

in Section 4; the paper closes with a discussion and planned extensions of this work.

2. SPH formulations

The SPH is a meshless method with Lagrangian nature [32, 38], and uses an interpolation technique to describe the continuum. It was originally developed for astrophysical purposes [19, 33] in the late 1970s. In this method, the computational domain is discretized into a finite number of integration points (also called particles) which carry material properties such as velocity, density, and stress, and move according to governing equations. The material properties of each particle are then calculated through the use of an interpolation process over its neighbouring particles [5]. This interpolation process is based on the integral representation of a field function. In the last four decades since the creation of the SPH method, its principal equations were derived and explained in several articles and books [30, 31, 36]. Therefore, the following description focuses on the features of SPH modified and tested within the presented study.

The final descritized form of the original integral representation of a field function can be written in the following form:

$$f(\boldsymbol{x_a}) = \sum_b m_b \frac{f_b}{\rho_b} W(r_{ab}, h) \tag{1}$$

where the subscript a denotes the integration point (particle), and the subscript b is for particles in the neighbourhood of the particle a, and r_{ab} is the distance between particles a and b. W is the kernel (smoothing function) which should satisfy numerous conditions as mentioned comprehensively in [31]. The field variables are m and ρ, which represent the mass and density of each particle, respectively. Details of the gradient approximation and other mathematical formulations of the SPH method are provided in Liu and Liu [31].

The choice of the kernel has impacts on the accuracy, efficiency, and stability of the SPH scheme. Kernels depend on the smoothing length, h, and the non-dimensional distance between particles, $q = r_{ab}/h$. The most well-known kernel (the cubic spline), which was proposed by Monaghan [37], is used in this study as follows:

$$W_{ab} = W(r_{ab}, h) = \alpha_d \begin{cases} 1 - \frac{3}{2}q^2 + \frac{3}{4}q^3, & 0 \le q \le 1 \\ \frac{1}{4}(2-q)^3, & 1 \le q \le 2 \\ 0 & q \ge 2 \end{cases} \tag{2}$$

where α_d is $10/(7\pi h^2)$ in 2D and $1/(\pi h^3)$ in 3D.

2.1. SPH for fluids

In SPH, incompressible fluids can be approximated by a slightly compressible fluid [37], and simulated in a straightforward way. Accordingly, the SPH scheme, considered in this study, is a Weakly Compressible SPH (WCSPH) [39]. The fundamental equations of fluid motion are the Navier-Stokes, which express the conservation of mass and momentum in the Lagrangian space. These equations can be rewritten in the SPH framework in the following forms:

the continuity equation:

$$\frac{d\rho_a}{dt} = \rho_a \sum_b \frac{m_b}{\rho_b} v_{ab}^{\alpha} \frac{\partial W_{ab}}{\partial x_a^{\alpha}}, \quad \text{where} \quad v_{ab}^{\alpha} = v_a^{\alpha} - v_b^{\alpha} \tag{3}$$

the momentum equation (for Newtonian fluids as described in Shao and Lo [44]):

$$\frac{dv_a^{\alpha}}{dt} = -\sum_b m_b \left(\frac{p_a}{\rho_a^2} + \frac{p_b}{\rho_b^2} \right) \frac{\partial W_{ab}}{\partial x_a^{\alpha}} + \sum_b \frac{4 m_b (\mu_a + \mu_b) v_{ab}^{\alpha}}{(\rho_a + \rho_b)^2} \left(\frac{1}{r_{ab}} \frac{\partial W_{ab}}{\partial r_{ab}} \right) + f_a^{\alpha} \tag{4}$$

where f^{α}, m, p, ρ, μ and v^{α} denote body force, mass, pressure, density, dynamic viscosity and velocity of each particle, respectively. It is noticeable that the subscripts a and b represent water particles in this paper.

The second summation of Eq. (4) is an estimation of the viscous shear force and is derived based on a mixture of a standard SPH first derivative and a finite difference approximation [44]. This formulation conserves linear momentum exactly while angular momentum is only approximately conserved.

As known in WCSPH, an equation of state (EOS) must be used to correlate density and pressure. The EOS used in this paper is proposed by Batchelor for water [37]:

$$p = \frac{\rho_0 c_s^2}{7}\left(\left(\frac{\rho}{\rho_0}\right)^7 - 1\right) \tag{5}$$

where c_s is the speed of sound; ρ_0 is the density at rest (initial condition). Taking the actual value of the sound speed produces large fluctuation in pressure field, and requires infinitesimal time step. As proposed by Monaghan [37], the speed of sound should be chosen slightly higher than $10u$, in which u is the highest velocity of the flow, to preserve density variations less than a percent and fulfill the weakly compressible assumption.

2.2. SPH for soils

The mass conservation equation (Eqs. (3) is still valid to approximate the density changes. However, the general form of the momentum equation is required to define the motion of soil particles:

$$\frac{d\boldsymbol{v}_i^\alpha}{dt} = \sum_j m_j \left(\frac{\sigma_i^{\alpha\beta}}{\rho_i^2} + \frac{\sigma_j^{\alpha\beta}}{\rho_j^2}\right)\frac{\partial W_{ij}}{\partial x_i^\beta} + \boldsymbol{f}_i^\alpha \tag{6}$$

where $\sigma^{\alpha\beta}$ is the stress tensor which consists of two parts: an isotropic pressure, p which was defined for fluids in Section 2.1, and the deviatoric shear stress, $s^{\alpha\beta}$,

$$\sigma^{\alpha\beta} = -p\delta^{\alpha\beta} + s^{\alpha\beta} \tag{7}$$

where $\delta^{\alpha\beta}$ is Kroneckers delta, $\delta^{\alpha\beta} = 1$ if $\alpha = \beta$ and $\delta^{\alpha\beta} = 0$ if $\alpha \neq \beta$. The isotropic pressure for soil particles can be calculated in two ways: an equation of state or a soil constitutive equation. These two ways were completely explained by Bui et al. [6], and the second approach, which is based on the stress-strain relationship, was used in this study as follows:

$$p = -\frac{\sigma^{\gamma\gamma}}{3} = K\epsilon^{\gamma\gamma} \tag{8}$$

where K is the bulk modulus; $\epsilon^{\gamma\gamma}$ is the volumetric strain which is a function of the actual soil displacements.

The second component in Eq. (7), which is the deviatoric shear stress, requires a proper soil constitutive equation. In this paper, an elastic-perfectly plastic model, as the soil constitutive model, will be used to simulate soil behaviour [9]. This soil model will be applied within the SPH framework by utilizing the hypo-elastic model [4] and an appropriate yield criterion for soils. This type of soil modelling was initially presented in Bui et al. [6] and extensively explained in Bui et al. [7]. The main equations will be provided in this paper, and further details of the derivation can be found in Chen and Mizuno [9] and Bui et al. [7].

The generalized Hooke's law can be employed to calculate stress-rate out of strain-rate. When considering a large deformation problem, a stress-rate that is invariant with respect to rigid-body rotation must be used (an objective stress-rate tensor). Accordingly, the Jaumann rate was utilized. Finally, the rate of stress can be written in the following form:

$$\dot{\sigma}^{\alpha\beta} - \sigma^{\alpha\gamma}\dot{\omega}^{\beta\gamma} - \sigma^{\gamma\beta}\dot{\omega}^{\alpha\gamma} = 2G\dot{e}^{\alpha\beta} + K\dot{\epsilon}^{\gamma\gamma}\delta^{\alpha\beta} \tag{9}$$

where $\dot{\epsilon}^{\gamma\gamma}$ and $\dot{e}^{\alpha\beta}$ are the volumetric and deviatoric strain-rates, respectively. Furthermore, $\dot{\epsilon}^{\alpha\beta}$ and $\dot{\omega}^{\alpha\beta}$ are the total strain-rate and rotation-rate tensors defined in SPH framework as:

$$\dot{\epsilon}^{\alpha\beta} = \frac{1}{2}\left(\frac{\partial v^\alpha}{\partial x^\beta} + \frac{\partial v^\beta}{\partial x^\alpha}\right) \Rightarrow \dot{\epsilon}_i^{\alpha\beta} = \frac{1}{2}\sum_j \left(\frac{m_j}{\rho_j}(v_j^\alpha - v_i^\alpha)\frac{\partial W_{ij}}{\partial x_i^\beta} + \frac{m_j}{\rho_j}(v_j^\beta - v_i^\beta)\frac{\partial W_{ij}}{\partial x_i^\alpha}\right) \tag{10}$$

$$\dot{\omega}^{\alpha\beta} = \frac{1}{2}\left(\frac{\partial v^{\alpha}}{\partial x^{\beta}} - \frac{\partial v^{\beta}}{\partial x^{\alpha}}\right) \Rightarrow \dot{\omega}_i^{\alpha\beta} = \frac{1}{2}\sum_j \left(\frac{m_j}{\rho_j}(v_j^{\alpha} - v_i^{\alpha})\frac{\partial W_{ij}}{\partial x_i^{\beta}} - \frac{m_j}{\rho_j}(v_j^{\beta} - v_i^{\beta})\frac{\partial W_{ij}}{\partial x_i^{\alpha}}\right) \tag{11}$$

where the subscripts i and j are used to describe soil SPH particles as opposed to water ones.

The flow plasticity theory is employed in this study to take into account the plastic behaviour of soils in large deformation. This theory is characterized by the assumption that a flow rule exists to determine the amount of plastic deformation in the material. For defining the onset of the plasticity, an appropriate yield criterion must be used, and plastic deformation occurs only when the stress path moves beyond the yield surface [9]. The Drucker-Prager method is chosen as the yield criterion, Y, in this study, and the yield surface is accordingly described by,

$$Y(I_1, J_2) = \sqrt{J_2} + \alpha I_1 = k \tag{12}$$

$$I_1 = \sigma^{xx} + \sigma^{yy} + \sigma^{zz} \quad \text{and} \quad J_2 = \frac{1}{2}s^{\alpha\beta}s^{\alpha\beta} \tag{13}$$

where I_1 is the first invariant of the stress tensor, and J_2 denotes the second invariant of the deviatoric stress tensor. α and k are Drucker-Prager's constants which can be derived from plane-strain condition as,

$$\alpha = \frac{\tan\phi}{\sqrt{9 + 12\tan^2\phi}} \quad \text{and} \quad k = \frac{3c}{\sqrt{9 + 12\tan^2\phi}} \tag{14}$$

where c and ϕ are the cohesion and internal friction angle of soil, respectively. Since the non-associated flow rule in the flow plasticity theory is utilized in this study, a plastic potential function, g, is required which can be defined by,

$$g = \sqrt{J_2} + 3I_1\sin\psi \tag{15}$$

where ψ is the dilatancy angle, and zero dilatancy angle represents that the material is plastically incompressible.

Finally, the soil constitutive equation for particle i in the SPH form can be summarized as [7, 9],

$$\frac{d\sigma_i^{\alpha\beta}}{dt} = \sigma_i^{\alpha\gamma}\dot{\omega}_i^{\beta\gamma} + \sigma_i^{\gamma\beta}\dot{\omega}_i^{\alpha\gamma} + 2G\dot{\epsilon}_i^{\alpha\beta} + K\dot{\epsilon}_i^{\gamma\gamma}\delta^{\alpha\beta} - \dot{\lambda}_i\left[9K\sin\psi\delta^{\alpha\beta} + \frac{G}{\sqrt{J_2}}s_i^{\alpha\beta}\right], \tag{16a}$$

$$\dot{\lambda}_i = \frac{3\alpha K\dot{\epsilon}_i^{\gamma\gamma} + (G/\sqrt{J_2})s_i^{\alpha\beta}\dot{\epsilon}_i^{\alpha\beta}}{27\alpha K\sin\psi + G} \tag{16b}$$

where $\dot{\lambda}$ is the rate of the so-called plastic multiplier, λ, which is dependent on the state of stress and load history. Eqs. (3) and (6) in conjunction with Eq. (16a) can express the soil behaviour as an elastic-perfectly plastic material. However, due to numerical errors during computations, which are commonly found in computational plasticity, the stress state of soil may leave the elastic range. In such a circumstance, a return mapping algorithm is often used to numerically return the stress state to the yield surface. Refer to Bui et al. [7] and Chen and Mizuno [9] for further details.

The accuracy but also the capability of a numerical model for simulating realistic mechanical behaviour and deformations of soils depends on the definition of the initial stress condition. In this paper, the recommended approach by Bui and Fukagawa [5], which is based on the Linear Viscous damping concept, is used to avoid large stress fluctuation due to the self-weight gravity loading method.

2.2.1. Artificial stress

The tensile instability [45], which is a well-known difficulty in SPH, can be observed in problems dealing with cohesive soils since tensile stresses are likely produced in these problems. The tensile instability can be eliminated by introducing a short-range artificial force between particles as intensively explained in Gray et al. [22]. This procedure may be generalised to solid bodies if an artificial stress is defined in the stress tensor of each particle. The artificial stress, $R_i^{\alpha\beta}$, is added to the components of the stress tensor which were in tension. Therefore, the principal stresses, $\bar{\sigma}_i^{\gamma\gamma}$, should be utilized to determine whether the material is in tension or compression. Then, the principal artificial stress, $\bar{R}_i^{\alpha\beta}$, as shown in Eq. (17), should be added

only to those principal stresses which are positive (indicating tension). Finally, the artificial stress in the original coordinates is calculated by rotating the coordinates back.

$$\bar{R}_i^{\alpha\beta} = \begin{cases} -\epsilon \dfrac{\bar{\sigma}_i^{\alpha\beta}}{\rho_i^2}, & \alpha = \beta \\ 0 & \alpha \neq \beta \end{cases} \tag{17}$$

In the SPH momentum equation (Eq. (6)), the artificial stress should be placed next to the particles' stress as follows:

$$\left(\frac{\sigma_i^{\alpha\beta}}{\rho_i^2} + \frac{\sigma_j^{\alpha\beta}}{\rho_j^2} \right) \Rightarrow \left(\frac{\sigma_i^{\alpha\beta}}{\rho_i^2} + \frac{\sigma_j^{\alpha\beta}}{\rho_j^2} + R_{ij}^{\alpha\beta} f_{ij}^n \right) \tag{18}$$

where $R_{ij}^{\alpha\beta}$ and f_{ij} are defined by,

$$R_{ij}^{\alpha\beta} = R_i^{\alpha\beta} + R_j^{\alpha\beta} \quad \text{and} \quad f_{ij} = \frac{W(r_{ij})}{W(\Delta p)} \tag{19}$$

and Δp is particles spacing, which is a constant value, at the initial particles arrangement, and n in Eq. (18) and ϵ in Eq. (17) are constant values. Based on the dispersion equations [22], these values are determined 4 and 0.3, respectively. Nonetheless, Bui et al. [7, 8] recommended 2.55 and 0.5 for cohesive soils.

2.3. Artificial viscosity

To avoid non-physical oscillations in the case of shock wave modelling [31] and to prevent unphysical penetration of particles approaching each other [29]an artificial viscosity was developed by Monaghan [35, 40, 41], which is the most widely used so far in the SPH literature. This artificial viscosity is formulated as follows [16]:

$$\Pi_{ab} = \begin{cases} \dfrac{-\alpha \bar{c}_{ab} \mu_{ab} + \beta \mu_{ab}^2}{\bar{\rho}_{ab}^2}, & \boldsymbol{v}_{ab} \cdot \boldsymbol{x}_{ab} < 0 \\ 0 & \boldsymbol{v}_{ab} \cdot \boldsymbol{x}_{ab} \geq 0 \end{cases} \tag{20}$$

where α and β are constant coefficients which can vary in the range of 0 to 1. μ_{ab}, $\bar{c}_{ab}$ and $\bar{\rho}_{ab}$ are defined by,

$$\mu_{ab} = \frac{h_{ab} \boldsymbol{v}_{ab} \cdot \boldsymbol{x}_{ab}}{r_{ab}^2 + 0.1 h_{ab}} \quad , \quad \bar{c}_{ab} = \frac{1}{2}(c_a + c_b) \quad \text{and} \quad \bar{\rho}_{ab} = \frac{1}{2}(\rho_a + \rho_b) \tag{21}$$

$$\boldsymbol{v}_{ab} = \boldsymbol{v}_a - \boldsymbol{v}_b \quad , \quad \boldsymbol{x}_{ab} = \boldsymbol{x}_a - \boldsymbol{x}_b \quad \text{and} \quad h_{ab} = \frac{1}{2}(h_a - h_b) \tag{22}$$

and $\boldsymbol{x}$ is the particle position vector.

The artificial viscosity term should be added to Eq. (18) for soils (see Eq. (23)). For fluids, the pressure part of Eq. (4) should be modified as per Eq. (24). Although the fluid viscosity is considered in Eq. (4), $\alpha = 0.05$ and $\beta = 0$ were used to avoid any unphysical penetration of particles in results. As per the suggestion by Bui et al. [7], α and β were considered to be 0.1 for soils in this study.

$$\left(\frac{\sigma_i^{\alpha\beta}}{\rho_i^2} + \frac{\sigma_j^{\alpha\beta}}{\rho_j^2} + R_{ij}^{\alpha\beta} f_{ij}^n \right) \Rightarrow \left(\frac{\sigma_i^{\alpha\beta}}{\rho_i^2} + \frac{\sigma_j^{\alpha\beta}}{\rho_j^2} + R_{ij}^{\alpha\beta} f_{ij}^n + \Pi_{ij} \delta^{\alpha\beta} \right) \tag{23}$$

$$\left(\frac{p_a}{\rho_a^2} + \frac{p_b}{\rho_b^2} \right) \Rightarrow \left(\frac{p_a}{\rho_a^2} + \frac{p_b}{\rho_b^2} + \Pi_{ab} \right) \tag{24}$$

2.4. Soil-water interaction

When water infiltrates the pore structure formed by soils (Fig. 1a), it applies some forces on the solid skeleton as shown in Fig. 1b. These forces can be divided into the buoyancy and seepage forces [26]. In the hydrostatic condition (Fig. 1c), the net force is the buoyancy force, $LA\gamma_w$, which always acts upward. Thus, the effective stress, σ', on the bottom of the soil sample can be calculated by,

$$\sigma' A = LA\gamma_s - LA\gamma_w \Rightarrow \sigma' = L\gamma_s - L\gamma_w \quad \text{or} \quad \sigma' = L(\gamma_s - \gamma_w) \tag{25}$$

where A is the soil sample area. γ_s and γ_w denote the unit weight of the saturated soil and water, respectively, and $\gamma_b = \gamma_s - \gamma_w$ is called the submerged (buoyant) unit weight of soil. As a result, the effective stress can be directly obtained using the submerged unit weight ($\sigma' = L\gamma_b$) [26] instead of the total stress minus the pore water pressure ($\sigma' = \sigma - u_w$).

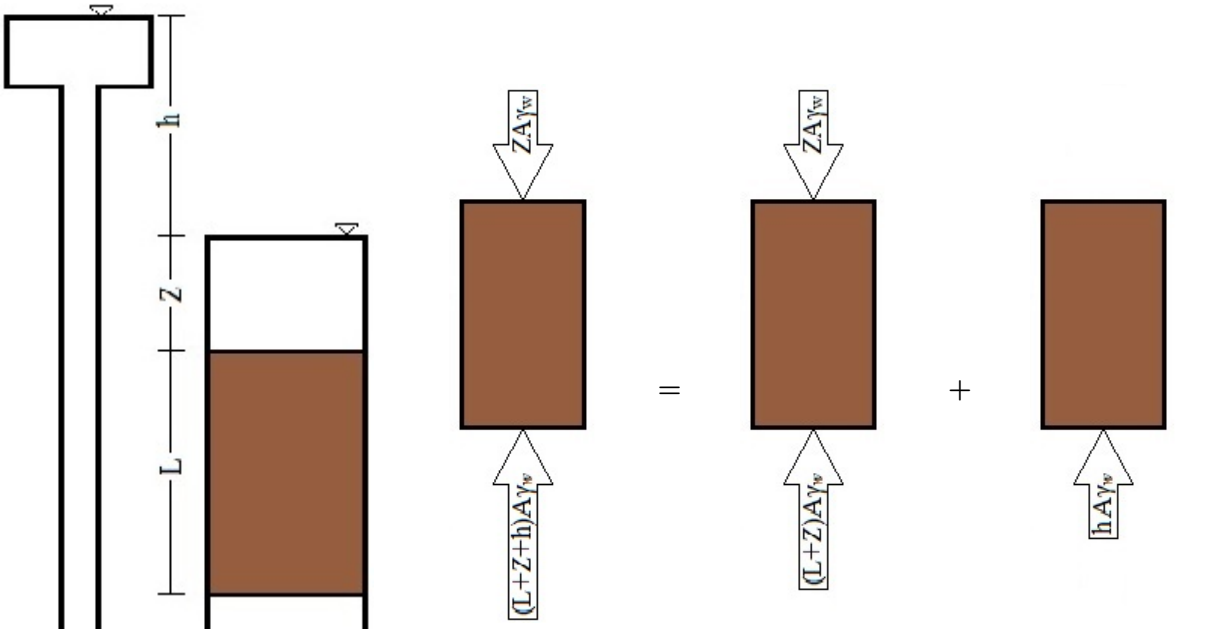

(a) A Soil sample with a seepage flow

(b) Total boundary forces

(c) Buoyancy forces

(d) Seepage forces

Figure 1: Schematic view of a soil sample with body forces diagrams

The seepage force, as illustrated in Fig. 1d, is applied to the soil particles in the direction of flow. A proper expression for this force is the force per unit of volume of soil as,

$$\boldsymbol{f}_{seepage} = \frac{\text{Seepage force}}{\text{Volume of soil}} = \frac{hA\gamma_w}{LA} = i\gamma_w \tag{26}$$

where i is the hydraulic gradient, $i = \frac{h}{L}$. In porous media, Darcy's law, $i = \frac{v}{k}$, is valid in laminar flow condition, so Eq. (26) can be modified as follows:

$$\boldsymbol{f}_{seepage} = \frac{\boldsymbol{v}}{k}\gamma_w = \frac{(\boldsymbol{v}_{water} - \boldsymbol{v}_{soil})}{k}\gamma_w \tag{27}$$

where k denotes the hydraulic conductivity of soil and $\boldsymbol{v}$ is the velocity vector. However, the Forchheimer equation, $i = a\boldsymbol{v} + b|\boldsymbol{v}|\boldsymbol{v}$, considers the microscopic inertial effect for transient and turbulent flow conditions

by adding a quadratic velocity term to Darcy equation. Therefore, Eq. (26) can be rewritten as:

$$\boldsymbol{f}_{seepage} = a(\boldsymbol{v}_{water} - \boldsymbol{v}_{soil})\gamma_w + b|\boldsymbol{v}_{water} - \boldsymbol{v}_{soil}|(\boldsymbol{v}_{water} - \boldsymbol{v}_{soil})\gamma_w \tag{28}$$

Several empirical and semi-empirical formulae have been derived from measurements for the coefficients a and b [46]. In this study, the approach of Den Adel [11] was used, which defines the coefficients as follows:

$$a = \alpha \frac{(1-n)^2}{n^3} \frac{\nu}{gD_{15}^2} \quad \text{and} \quad b = \beta \frac{1}{n^2} \frac{1}{gD_{15}} \tag{29}$$

where n, g, ν and D_{15} are the soil porosity, gravity acceleration, water kinematic viscosity and effective particle size, respectively. α lies between 75 to 350, and β can vary from 0.9 to 5.3 for different soil samples.

In this study, problems are divided into two distinct SPH domains: water and soil. The interaction between these two phases is defined by introducing two components: the seepage force and the effective stress using the submerged unit weight concept as discussed above. The seepage force (Eqs. (27) or (28)) will be simply placed in the momentum equations of the both soil and water particles (Eqs. (30) and (31)).

In order to calculate the effective stress, the Linked-Cell-List method (refer to Section 2.6), which is used to find the neighbour particles, is utilized to find saturated soil particles. It is noteworthy to mention that the presented scheme is only able to simulate fully saturated and dry soil conditions (not unsaturated soil condition). To distinguish a saturated soil particle from a dry one, the following procedure is repeated for all soil particles within a model at each time step. If any water particles exist in the linked-cell of a soil particle and the vertical location of one of these water particles is above the vertical position of the soil particle, that soil particle is identified as a saturated soil particle. Afterward, the initially assigned dry unit weight, γ_d, and the corresponding mass, m_d, of the identified saturated soil particle will be changed to the submerged unit weight, γ_b, with a new mass, m_s, by considering the same particle volume ($V/g = \frac{m_d}{\gamma_d} = \frac{m_s}{\gamma_b}$). Hence, the mass and density of soil particles are dynamically switching between the dry or submerged conditions by varying water table. It is noticeable that ρ^s will be used in the rest of paper to denote this switching density based on the explained approach.

It is well-known that WCSPH suffers from pressure fluctuations. One of the reasons for providing this approach is to avoid undesirable impacts of pressure fluctuations in results. However, the main advantage of this approach is to be able to simulate problems where the water table is above the ground surface (fully submerged structures). In these problems, the obtained pore water pressure as the result of the water domain is usually overestimated, with the consequence that the effective stress will be underestimated.

It is noticeable that the total stress cannot be acquired directly from this introduced framework, and the pressure of water particles at each point represents the pore water pressure directly. Therefore, the total stress can be calculated by adding the pore water pressure to the obtained effective stress (reverse calculation).

Finally, the motion of SPH particles on each domain is solved separately using its own SPH governing equations (see Sections 2.1 and 2.2). The final momentum equations for each phase can be summarised as:

the momentum equation for the soil phase

$$\frac{dv_i^\alpha}{dt} = \sum_j m_j \left(\frac{\sigma_i'^{\alpha\beta}}{\rho_i^{s\ 2}} + \frac{\sigma_j'^{\alpha\beta}}{\rho_j^{s\ 2}} + R_{ij}^{\alpha\beta} f_{ij}^n + \Pi_{ij}\delta^{\alpha\beta} \right) \frac{\partial W_{ij}}{\partial x_i^\beta} + f_i^\alpha + \sum_a m_a \frac{f_{ia}^{seepage\ \alpha}}{\rho_i^s \rho_a} W_{ia} \tag{30}$$

the momentum equation for the water phase

$$\frac{dv_a^\alpha}{dt} = -\sum_b m_b \left(\frac{p_a}{\rho_a^2} + \frac{p_b}{\rho_b^2} + \Pi_{ab} \right) \frac{\partial W_{ab}}{\partial x_a^\alpha} + \sum_b \frac{4m_b(\mu_a + \mu_b)v_{ab}^\alpha}{(\rho_a + \rho_b)^2} \left(\frac{1}{r_{ab}} \frac{\partial W_{ab}}{\partial r_{ab}} \right) + f_a^\alpha - \sum_i m_i \frac{f_{ia}^{seepage\ \alpha}}{\rho_i^s \rho_a} W_{ia} \tag{31}$$

where the subscripts i and j represent soil particles while a and b are used for water particles.

2.5. Boundary conditions

Solid bodies, such as walls, are built with parallel layers of immovable particles (fixed in place) acting as a solid boundary [10]. Basically, solid boundary particles are fixed fluid or soil particles that contribute to the continuity and momentum evolution, but they are not allowed to move. Accordingly, forces acting on a solid wall can be directly calculated by summing up the momentum equation (Eqs. (30) and (31)) over all fixed boundary particles multiplied by their masses. Number of layers depends on kernels to avoid the kernel support truncation of free particles, which are very close to the solid boundary, because the truncation produces some errors in estimating of key variables, such as the density. It is noticeable that solid boundaries must be defined for each phase (soil and fluid) separately. The most significant advantage of this approach is that the computational treatment of the system is considerably simplified since no special considerations are necessary for solid boundary particles. The proposed approach by Adami et al. [1], which is based on smoothed velocity and stress fields, is used to enforce the no-slip condition on solid wall boundaries.

The in/out-flow boundary condition, which was proposed by Federico et al. [13], was used to inject water within the fluid domain. Further details of the computational procedure are reported in Gholami Korzani et al. [18].

The periodic boundary condition is employed [17] to model a soil stratum perpendicular to the gravity direction in Section 3. This type of boundary condition was implemented by considering that particles located at a boundary are linked to particles at the opposite boundary. Therefore, a particle that leaves a boundary immediately re-enters at the opposite boundary with the same velocity.

2.6. Time integration

Eqs. (3), (16a), (30) and (31) constitute the complete set of equations for both soil and water phases to be solved by integrating in time. Accordingly, an open source code, called PersianSPH[1], has been developed in C++ on Linux platform, and whole computations were done in parallel by using the OpenMP library. In each step, the Linked-Cell-List approach [23] is used to search neighbouring particles in order to find interacting particle pairs. Afterward, forces between interacting pairs of particles are calculated, and eventually, the field variables at each particle are updated using a modified Verlet explicit integrator scheme [3]. For stability of the integration, several time step criteria must be satisfied as discussed in Morris et al. [42].

3. Validations

In the following, the introduced SPH scheme is validated using simplified geotechnical problems for which analytical solutions or experimental data exist. Altogether, three problems are considered: (1) gravitational flow following a soil collapse under dry condition will be simulated and compared with available experimental data to prove the capability of the model to predict large deformations, (2) the hydrostatic pore water pressure and the effective stress will be examined to verify the correctness of the second component (the effective stress concept using the submerged unit weight) in the interaction method (see Section 2.4), and (3) the seepage flow in a column and the identification of the phreatic surface within an embankment will be used to testify the first component (the seepage force) in the interaction method (see Section 2.4).

3.1. Post-failure behavior of granular material at dry condition

The experimental study published by Bui et al. [7] was used as a benchmark to individually verify the performance of the used soil model. In this experiment, the collapse of granular material on a flat surface is investigated as a 2D problem by using straight aluminium rods as a substitute for non-cohesive soil. A $20x10cm$ rectangular soil sample was built using these rods in a box with movable walls. The failure of the sample was initiated by quickly removing the right wall of the box horizontally. Bui et al. [7] have used these experiments as well to validate their numerical model. For this purpose, the mechanical parameters of

[1] http://korzani.wixsite.com/persiansph

the aluminum rods have been quantified by means of modified standard tests such as shear box tests. Based on these tests the friction angle was determined to be 19.8°, and the averaged bulk modulus, assuming a constant Poisson's ratio of 0.3, was determined to be $0.7MPa$. The cohesion coefficient $c = 0$ was determined based on the stress-strain curve.

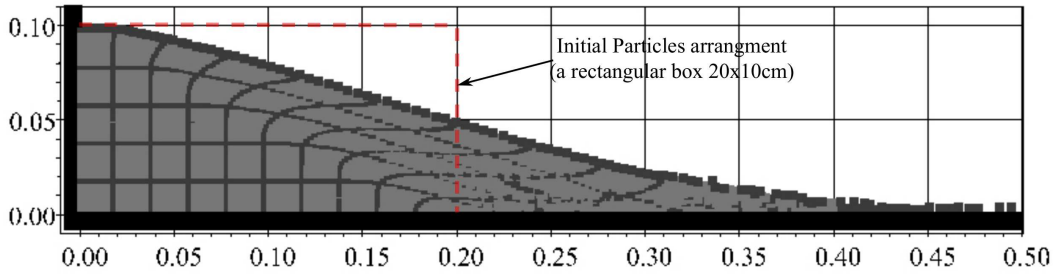

(a) SPH simulation result and the model initial condition

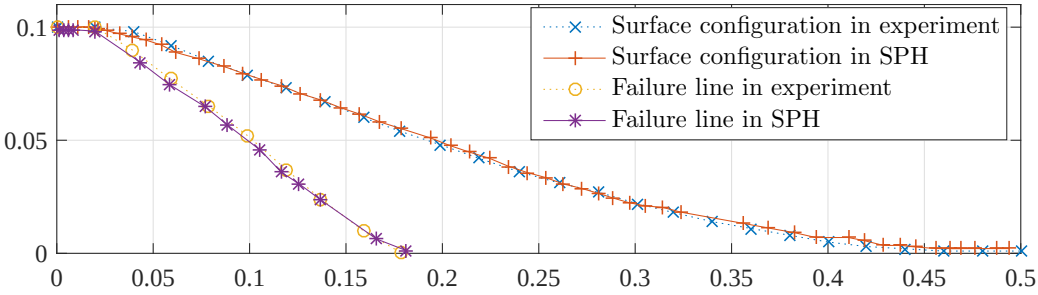

(b) Final surface configurations and failure lines in the experiment and the simulation

Figure 2: Comparison between the experiment and SPH simulation of non-cohesive granular soil failure

For the numerical simulation using the presented model, the non-associated flow rule soil model with $\psi = 0$ was employed. The tensile instability correction was not utilized as the non-cohesive soil was modelled. Furthermore, no-slip solid boundary condition was applied to model the existence of the fixed walls. As shown in Fig. 2, a very good agreement between simulation and experimental results [7] is achieved. Not only the overall deformation was matched using the SPH model, but the failure line, which represents the transition from the non-moving part of the sample to the deforming soil body, could be also identified. This result proves that the presented model is capable of simulating large soil deformations and the zones for shear deformation within a dry soil body.

3.2. Fully and partly submerged soil sample subject to the gravitational loading

In order to consider the effective stress concept in coupled hydro-mechanical problems, a new approach using the submerged unit weight was provided in Section 2.4. To prove the presented approach for correctly simulating the effective stress, a soil sample with $1m$ depth is simulated in two hydrostatic conditions: a) the water table at $0.4m$ above the ground surface and b) the water table at $0.4m$ below the ground surface (see Fig. 3). The soil behaviour was assumed to be elastic with the following properties: $E = 15MPa$, $\nu = 0.3$, $\gamma_{sat} = 20$ kN/m^3, and $\gamma_w = 9.98$ kN/m^3. According to the elastic soil behaviour and the assumed Poisson ratio, the lateral earth pressure coefficient at rest K_0 is approximately 0.43. Based on these properties and assumptions, the effective vertical and horizontal stresses and pore water pressure can be easily calculated with the well-known equations for geostatic conditions.

For the simulations, the periodic boundary was used in the horizontal direction to replicate a soil stratum of vast length. In addition, no-slip solid boundary condition was employed at the bottom of the sample representing an impermeable rock bed. Gravity was imposed in the vertical direction. Fig. 3 illustrates the

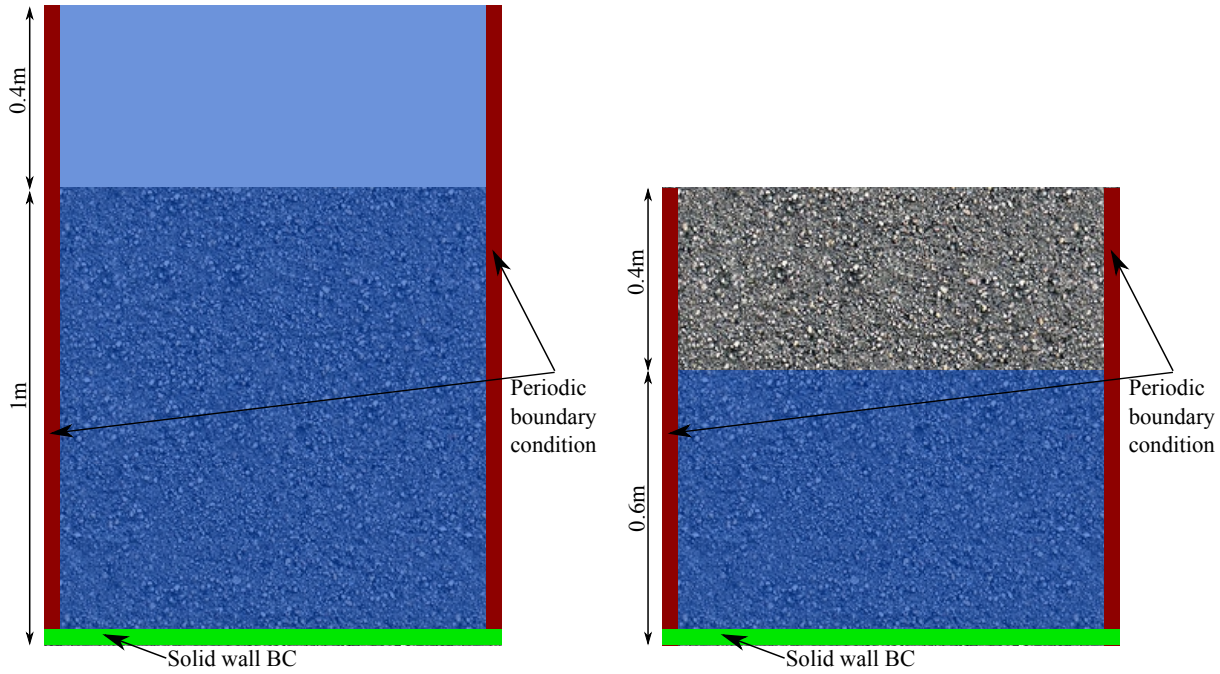

(a) fully submerged soil sample

(b) partly submerged soil sample

Figure 3: Geometries and boundary conditions of test samples

geometries and boundary conditions of the considered models. In total, 2520 particles were deployed for the fully submerged model while 1720 particles were used for the partly submerged model. The smoothing length was chosen to be $0.026m$ for both simulations.

The modelling and simulation processes are explained in the following to better understand how the presented approach practically works. It is not pre-defined which part of a model is saturated. The soil domain is initially modelled as a dry soil with its own properties; when the interaction part of the code is started, the saturated part of the soil domain will be identified at each time step. Then, the properties of this saturated part will automatically be changed to the submerged condition as explained in Section 2.4. The total stress is not directly calculated within the model as the effective stress is the primary output of the code. Subsequently, the pore water pressure from the pressure field of the water domain can be obtained. If the total stress is required, the effective stress and pore water pressure should be summed up in a subsequent post processing step. The initial and final densities of soil particles are plotted in Fig. 4 to further illustrate these processes.

As evident through Fig. 5, the obtained pore water pressures and effective vertical and horizontal stresses match perfectly with the results of analytical solutions. It is noticeable that water particles were initialized in these tests based on the recommendation of Monaghan [37] for setting up an initial density condition, and there is no water flow. Therefore, pressure fluctuations are negligible in the obtained pore water pressures in Fig. 5. Nevertheless, the pressure fluctuation is definitively an issue in WCSPH. However, there are methods to overcome this problem such as δ-SPH and Shepard filter [2, 43]. The Shepard filter is implemented in the presented code, but was not required to be used for the presented study.

This result shows clearly that the both SPH domains for fluid and solid correctly interact with each other resulting in the correct quantification of the effective stresses which finally are causative for deformations and failures of soil body.

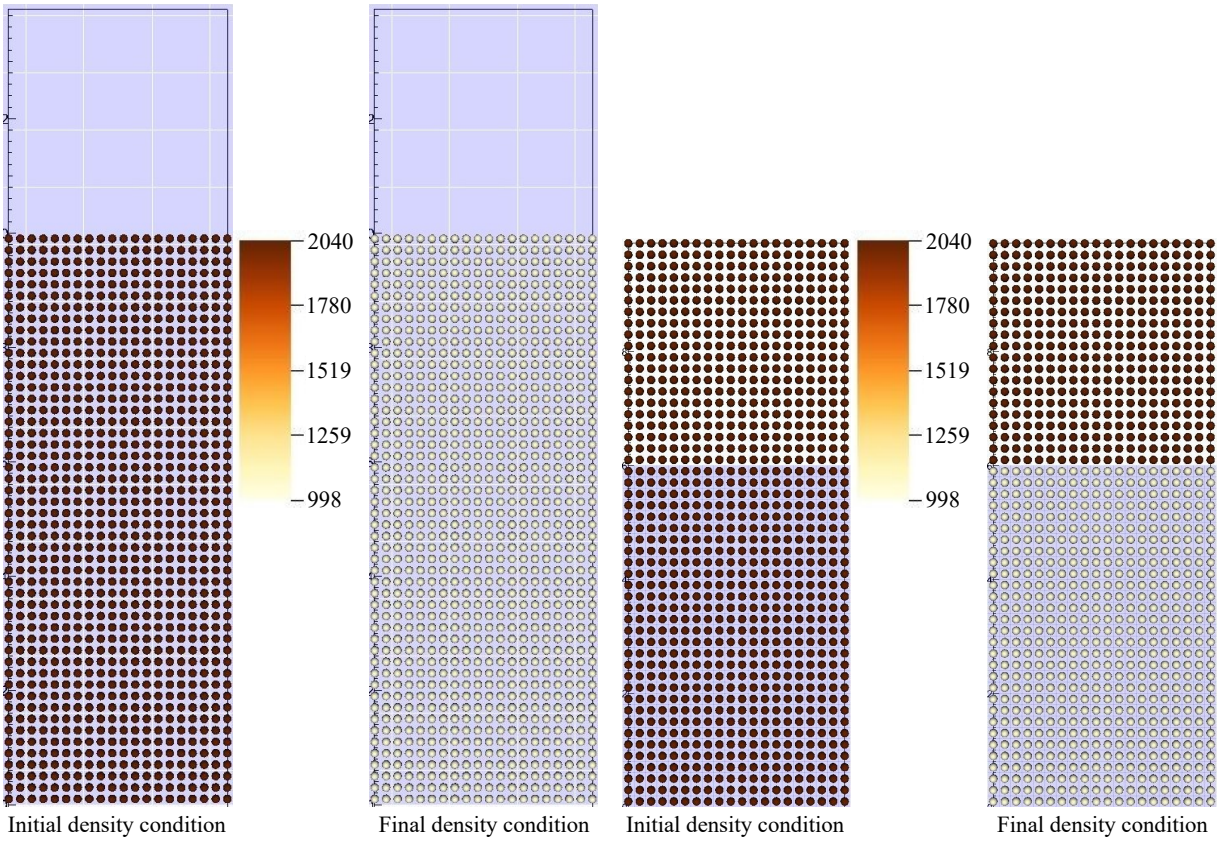

(a) fully submerged soil sample (b) partly submerged soil sample

Figure 4: Density evolution in the interaction module (the light blue color shows water phase while the filled spheres illustrate soil phase particles. The spheres color represents the density as shown in the legend of the figures.)

3.3. Seepage force for laminar and turbulent flow conditions

The considered problem of the stability of embankments under hydraulic loading requires the correct representation of the flow conditions within the porous medium. The force created by the seepage flow is finally causative for the failure of the embankment. As the seepage force cannot be directly determined through experiments, alternative experiments need to be considered to validate the used numerical model for correctly representing flow conditions in porous media. Two problems were studied depending on the considered flow conditions. The first experiment of this study is a column test for gravity-driven steady flow in the laminar flow range according to Darcy's law (Eq. (27)). The second experiment deals with flow through an embankment built of coarse-grained granular material which leads to partly-turbulent flow condition requiring the Forchheimer equation.

3.3.1. Laminar flow through a vertical column

A sand column with $4m$ height was considered in this simulation (Fig. 6a). The hydraulic conductivity of the soil was assumed to be $5 \times 10^{-2} m/s$. The soil particles were fixed in place while the movable water particles were subjected to gravity driving the flow in vertical direction downwards. Altogether 1440 particles, including soil and water particles, were used for this simulation. The periodic boundary in the horizontal direction was applied to model a laterally wide soil layer. In addition, the periodic boundary condition in the vertical direction was deployed to generate a continuous steady flow in the direction of gravity. Since the flow is driven by gravity only, the hydraulic gradient is $i = 1$. Therefore, the steady state

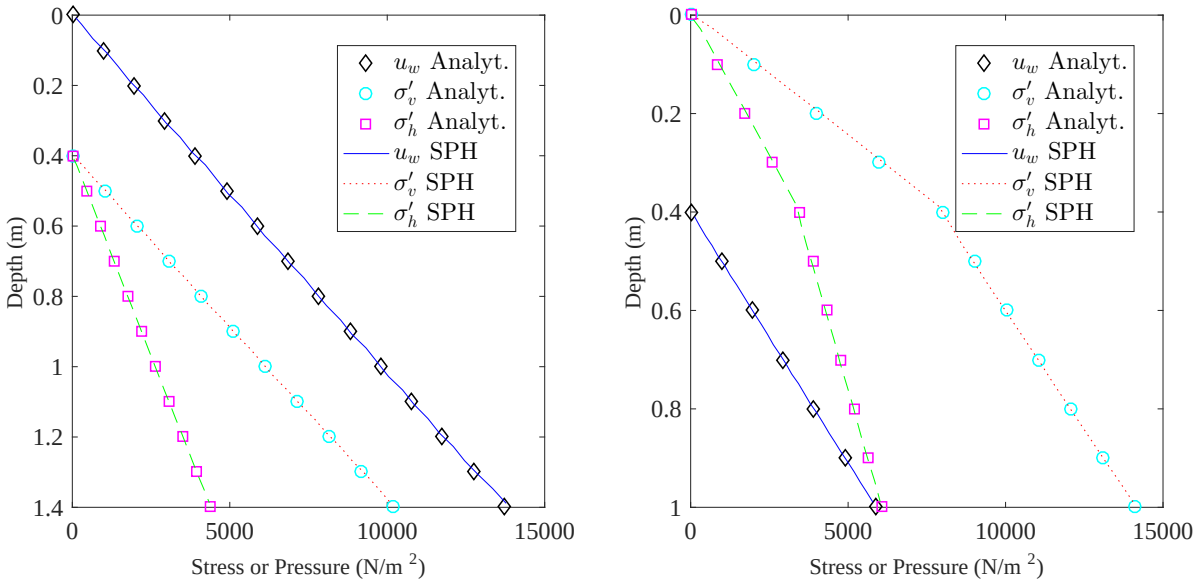

(a) fully submerged soil sample

(b) partly submerged soil sample

Figure 5: Comparison of the pore water pressure, vertical effective stress σ'_v and horizontal effective stress σ'_h between SPH results and the theoretical solution for the both soil samples

velocity of water particles should be $5 \times 10^{-2} m/s$ based on Darcy's law. Fig. 6b shows the average velocity of the water particles in time. The velocity deviation between the presented SPH results and analytical solution (based on Darcy's law) is less than 0.04%. As a consequence, the resulting seepage force defined in (Eq. (27)) as an interacting force can be considered to be realistically determined for laminar flow condition.

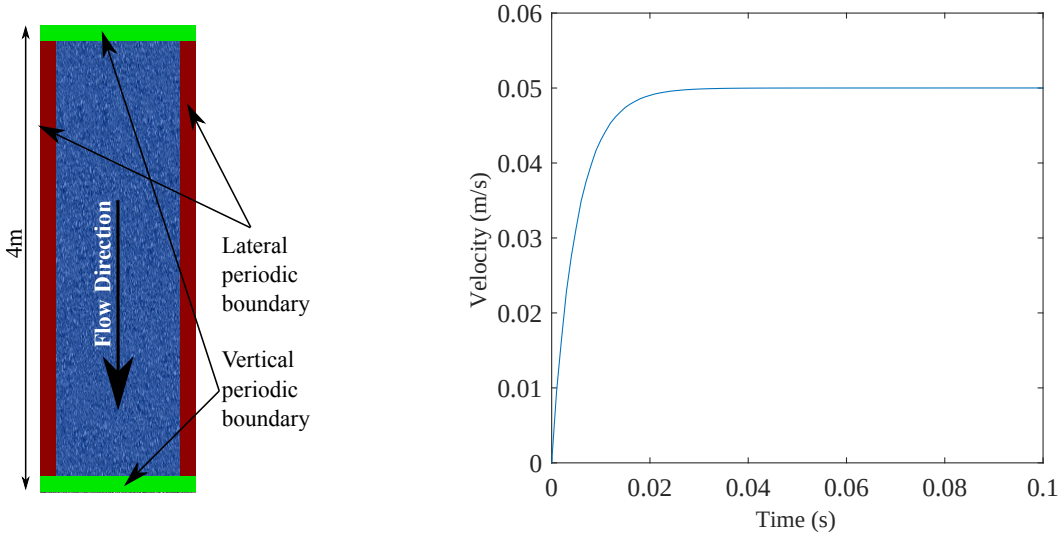

(a) Numerical setup

(b) Water velocity field

Figure 6: Model schematic sketch and velocity field of the vertical column

3.3.2. Phreatic surface in an embankment at turbulent flow condition

Experiments using a soil with high hydraulic conductivity were deliberately chosen to be able to calibrate the coefficients of Den Adel in Eq. (29) to be used in Eq. (28) for parametrising Forchheimer's flow law. Experiments conducted by Larese et al. [28] were used to calibrate and validate the capability of the SPH model to correctly represent turbulent flow conditions. In these experiments, a rock-fill embankment was built in a flume with a gravel of $D_{15} = 25.5mm$ and a porosity of the packing of $n = 0.41$ (see Larese et al. [28] for further details). Pressure sensors were installed in the bottom of the flume to determine the position of the phreatic surface within the embankment. The embankment was tested for different flow rates which were imposed on the upstream side. Two experiments of the study of Larese et al. with two different flow rates were considered for the validation of the presented model. While one experiment was used to quantify the parameters in Eq. (29), the second experiment served as a test case for the parametrised model. The dimensions of the embankment model created for the simulations matched the dimensions of the model in the experiments (see the green dashed line in Fig. 7). In/out-flow boundary condition was utilized in a way to generate the same flow conditions as in the experiments. The soil particles were fixed in place, and water particles were generated at the in-flow boundary with a velocity that fulfilled the assigned flow rate. 5745 particles with $0.026m$ smoothing length were employed to model the embankment (soil particles) and water boundary particles. The number of free water particles was increasing since the in-flow boundary was dynamically generating particles at each time step. Finally, a total number of particles should reach a constant value as the steady state condition (the final phreatic surface) was achieved.

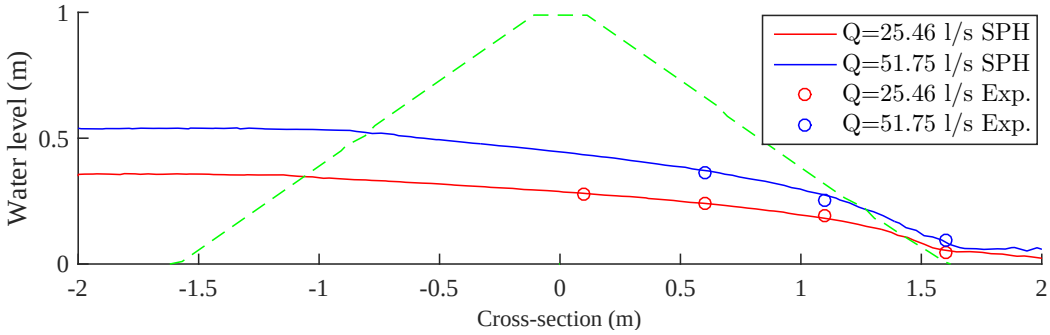

Figure 7: Phreatic surface for different flowrates

The flow rate of the experiment used for calibrating stage was $Q = 25.46l/s$. The resulting parameter α and β in Eq. (29) were obtained to be 150 and 0.4, respectively. It should be noted that β is not in the recommended range (see Section 2.4) suggested by Den Adel [46]. However, one needs to keep in mind that both parameters, α and β, have been determined originally based on experiments as well. Therefore, it is somewhat obvious that they can vary, probably even beyond the suggested range, depending on soil type, porosity, and particle size distribution (PSD). Nevertheless, a very good agreement between the simulation and experiment was achieved using these values for α and β (see the red line and symbols in Fig. 7). The same values were used to simulate, as a forecast, the experiment with a flow rate of $Q = 51.75l/s$. Also for this experiment, the agreement between the simulated and experimentally measured phreatic surface was very good (see the blue line and symbols in Fig. 7). Based on the results of this study and the good agreement between the simulation and experiment, it is justified to assume that the presented model will provide a realistic estimate of the seepage forces created by turbulent flow conditions.

4. Embankment under the influence of overburden load

4.1. Material parameters and dimensions

A homogeneous embankment with a height of $4m$ sitting on a foundation of $3m$ depth is considered for the numerical study on the hydro-mechanical behaviour of embankments influenced by an overburden load

(Fig. 8a). The inclination of both slopes of the embankment is 1 : 1.5 forming an angle of 33.7°. The width of the crest of the embankment is $3m$. A loading plate is placed centrally on the crest with a width of $2m$ to simulate the effect of a static overburden load. Soils with typical soil parameters have been chosen for embankment and foundation which were used and kept constant throughout the numerical study. The embankment is assumed to be built of a gravelly soil with high permeability while for the foundation a more sandy material is considered (see Tab. 1). For the simulation, the hydraulic conductivity is determined from D_{15} and the porosity using the well-known Forchheimer equation with Den Adel coefficients (Eqs. (28) and (29)).

Table 1: Soil properties of the embankment and its foundation

			Embankment	Foundation
Young modulus	E	MPa	25	50
Unit weight	γ	kN/m^3	18	20
Saturated unit weight	γ_s	kN/m^3	20	22
Porosity	n		0.35	0.25
Friction angle	ϕ	$degree$	30	20
Cohesion	c	kPa	8	10
Particle diameter	D_{15}	m	0.02	0.01

4.2. Considered scenarios, boundary conditions and simulation procedure

Four different scenarios with respect to hydraulic loading were considered: (1) completely dry condition without any effect of water (no fluid domain), (2) flood of moderate intensity, (3) severe flood, and (4) partly submerged condition (ponding on both sides of the embankment). The boundary conditions applied to the solid and fluid domains are shown in Fig. 8. While for the soil domain the side walls are assigned to be a free-slip boundary, the base is simulated as a no-slip boundary (Fig. 8a). For simulating the overburden load, the loading plate, which is a solid wall boundary in the soil phase, is vertically moving downward with a constant velocity, and the corresponding reaction force can be calculated as explained in Section 2.5. Therefore, the overburden load on the crest is applied as a displacement controlled loading. Fig. 8b shows the hydraulic boundary conditions used in scenarios (2) and (3). In these two scenarios, the foundation is considered to be fully submerged in the initial condition as can be seen on the assigned water table at the ground surface of the foundation. The side walls of the fluid domain in the foundation section are considered as free-slip boundaries and the base as a no-slip boundary. At the upstream side of the fluid domain, the side wall is extended to the complete height of the embankment providing an opening with a height of $1m$ as the in-flow boundary to enable the generation of water particles. At the downstream side above the foundation level, no wall existed allowing water particles to leave the domain. Fig. 8c shows the fluid domain for the simulation of scenario (4). In this scenario, the water table is simulated on both sides of the embankment with a height of $3.5m$ leaving a free-board of $0.5m$, and no water flow is initiated. Hence, the water tables on both sides are kept constant.

The simulation took place in a step-wise procedure: i) The initial soil stress condition is initiated by applying the damping force as introduced in Bui and Fukagawa [5]; ii) Using the hydraulic boundary conditions given in Fig. 8b, flow is generated until steady state phreatic surface is reached for scenarios (2) and (3). For scenarios (1) the soil domain is completely dry, so no fluid domain needs to be simulated. For scenario (4) no water is flowing, and the initial condition represents the steady state condition; iii) Once the steady state is hydraulically attained in the water domain, the loading step is commenced by moving the loading plate downwards, as explained above. The loading step is continued after failure to observe deformation and behaviour of the embankment in post-failure condition.

4.3. Results and discussion

After initializing the initial soil stress condition (see Sections 2.4 and 4.2), the assigned flow rates for scenarios (2) and (3), which are $Q = 0.25m^3/s$ and $Q = 0.5m^3/s$ (per one-meter length of the embankment),

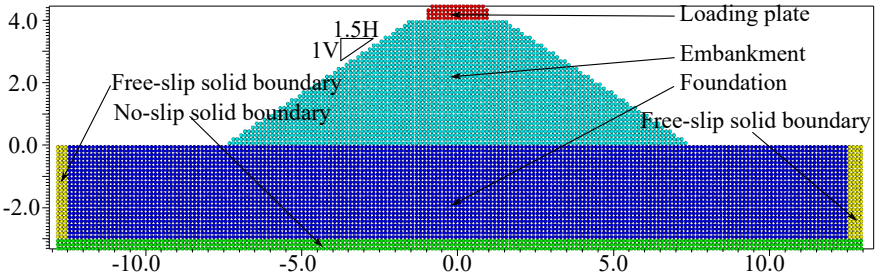

(a) Soil phase model

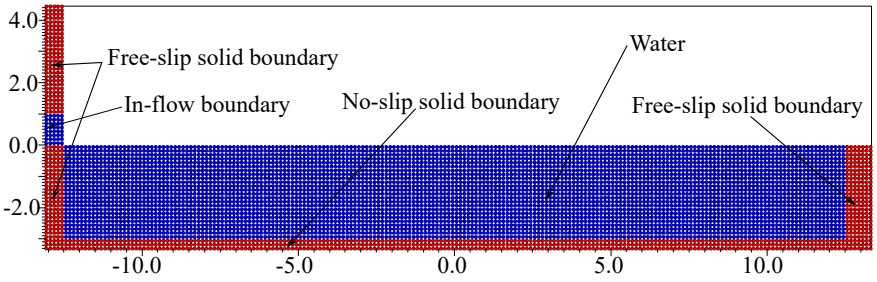

(b) Water phase model for the scenarios 2 and 3

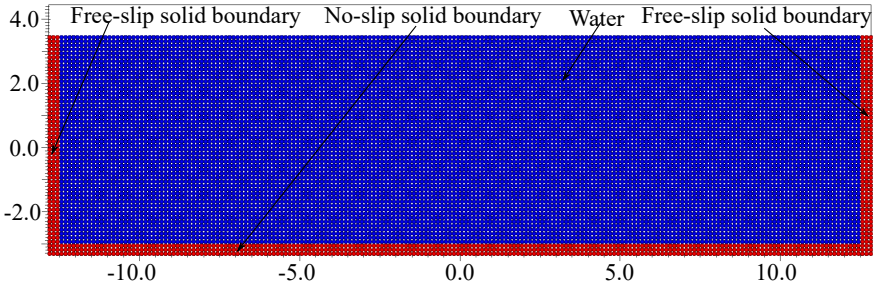

(c) Water phase model for the last scenario

Figure 8: Initial sketch of the embankment and the boundary conditions

were applied to the model. For scenario (2), Fig. 9 shows the evolution of the phreatic surface within the embankment in time before reaching the steady state (preparing the initial situation for applying the static traffic load). Finally, the resulting water levels upstream and downstream of the embankment as well as the phreatic surface within the embankment at steady state for the both flooding scenarios (2) and (3) are illustrated in Fig. 10 (the hydraulic equilibrium condition before the traffic load was applied). It should be noted that the Reynolds number within the embankment during transient infiltration has reached values of up to 1000 which is far beyond the laminar flow regime in a porous medium and proves the requirement of using the Forchheimer equation for simulating flow conditions occurring in these kinds of scenarios.

Since the aim was to study the bearing capacity of the embankment under the influence of water flow, the soil cohesion in the embankment was deliberately chosen high enough not to create any failure due to only water flow before applying the overburden load. Some deformations were visible in the embankment due to the water flow because the coupled two-phase model was used from the beginning of the simulations. As shown in Fig. 11, the flowing water in scenario (3) introduces some deformations at the downstream slope of the embankment, but the embankment is completely stable. In addition, the deformation patterns were different in all scenarios. To quantitatively compare deformations in all scenarios, the mean value of the equivalent deviatoric strain, which was 0.00115, was obtained for the dry condition immediately before applying the traffic load. Then, the area of the zone exceeding the equivalent deviatoric strain, as shown in Tab. 2, was calculated for all scenarios for the case immediately before applying the traffic load. The

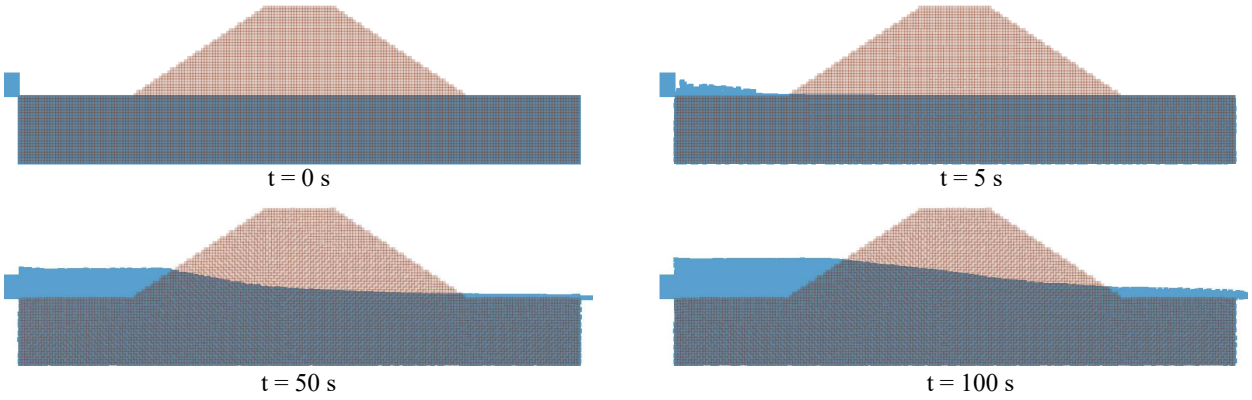

Figure 9: Water flow in the embankment at various time steps for $Q = 0.25m^3/s$

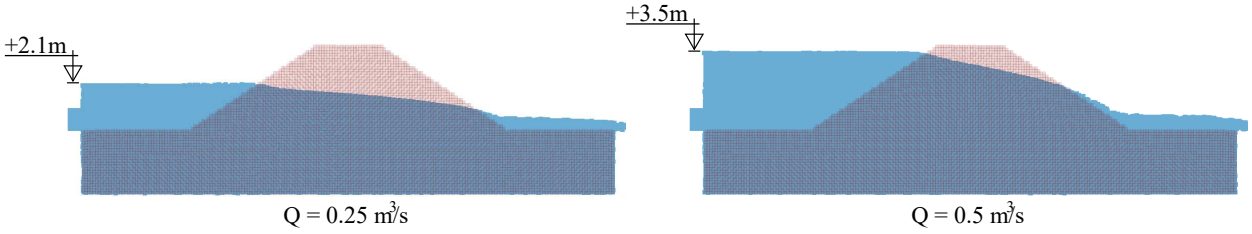

Figure 10: Water level in the embankment at the steady state

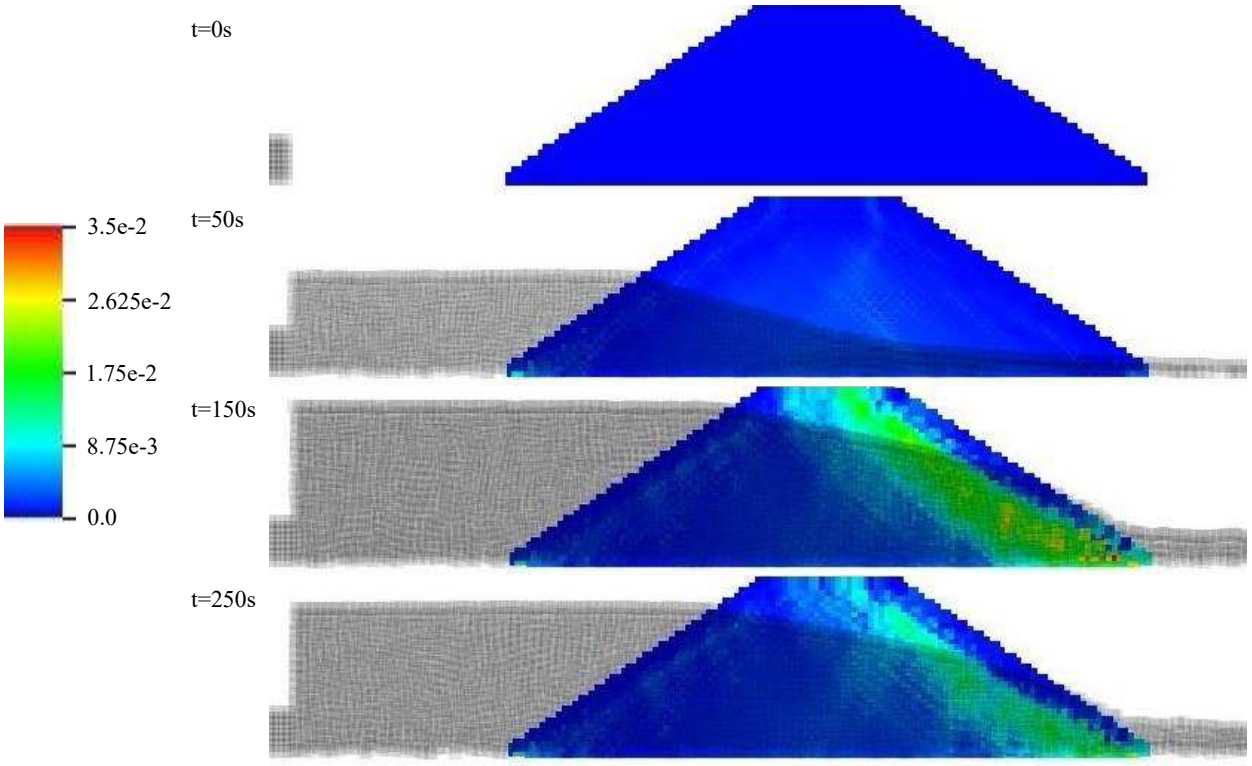

Figure 11: Equivalent deviatoric strain evolution for severe flood scenario (the gray shade illustrates water particles)

maximum equivalent deviatoric strain is also noted in the table for all scenarios. As illustrated in Fig. 12, the mean equivalent deviatoric strain is lower in the case of the partly submerged embankment since the effective stress is smaller due to hydrostatic pore water pressure. For the cases with flowing water, Fig. 12 demonstrates a large asymmetric area exceeding the equivalent deviatoric strain of the dry condition which is a clear indicator of the effect of the seepage force. If only hydrostatic pore water pressure would exist, the shear band before the load application should be similar to the results of Bui and Fukagawa [5].

Table 2: Comparing equivalent deviatoric strain in all scenarios

Scenarios	Dry	Partly submerged	Moderate flood	Severe flood
Avg. Eq. Dev. Strain	0.00115	0.00058	0.00174	0.00580
Zone area Exceeds 0.00115	41.1%	8.9%	67.7%	85.4%
Avg. Eq. Dev. Strain for Zone Exceeds 0.00115	0.00187	0.00125	0.00228	0.00667
Max. Eq. Dev. Strain	0.00294	0.00141	0.01309	0.03454

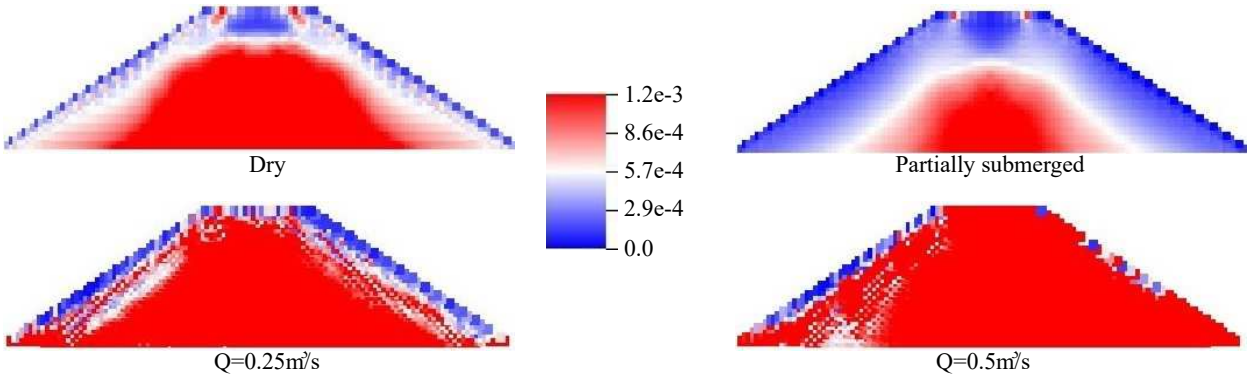

Figure 12: The highlighted equivalent deviatoric strain (red color) exceeding the mean value of the dry condition immediately before applying the traffic load

By applying the overburden load using the loading plate, the force-displacement curves for all scenarios given in Fig. 13 show at the beginning an almost linear increase which turned into a non-linear evolution after at latest $1.5cm$ displacement of the loading plate. After $6cm$ displacement, all scenarios produce a more or less constant loading force on different levels depending on the hydraulic situation. The highest residual loading force of approximately $220kN$ was reached with the dry embankment of scenario (1). Naturally, the embankment under extreme flood condition in scenario (3) shows the lowest residual loading force of $150kN$. It is visible in Fig. 13 that the dry condition produced a maximum in the loading force at a displacement of approximately $4.5cm$ characterising the exceedance of the maximum shear strength, which is in our simulations strongly influenced by changes in the geometry of the embankment. Likewise, the force-displacement curve for scenario (3) shows a distinct drop in the loading force to $100kN$ after $3cm$ displacement which is caused by the interplay between mechanical loading and seepage force at the toe of the downstream side slope. This drop is followed by an increase in the load bearing which is evidence of a new deformed stable geometry.

The observations of Fig. 13 can be partly explained by analysing the shear deformation within the embankment for the different scenarios at a stage where a more or less constant loading force was reached at $6cm$ plate displacement. As shown in Fig. 14, the fully dry embankment shows a symmetrical evolution of the shear deformation within the embankment. Under submerged conditions for scenario (4), which basically means under the influence of the buoyancy, the shear deformation is also symmetric, but with shear planes which have not fully reached the surfaces of the slopes. In this scenario, the existence of the pore water pressure, which was simulated as the buoyancy force in the model, reduced the effective stress, so the shear strength was reduced as evident in Fig. 13. Under the influence of water flow for scenario (2)

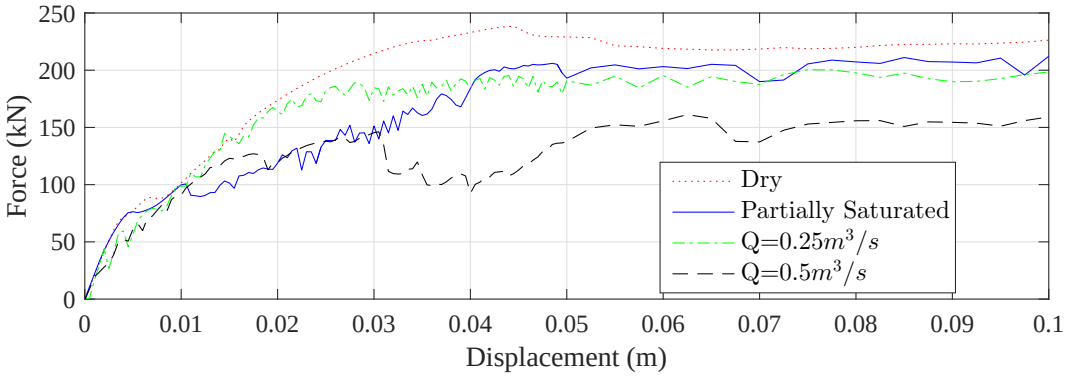

Figure 13: Force-displacement curves for all scenarios

and (3), the shear deformation becomes clearly non-symmetric. While for scenario (2) an incomplete shear plane still develops towards the upstream side together with another shear plane at the downstream side slope, the shear deformation for a higher flow rate in scenario (3) reveals clearly only one sliding slope at the downstream side. In scenario (3), the green shaded area close to the surface of the downstream side of the embankment indicates deformations caused by the seepage force due to high flow velocity.

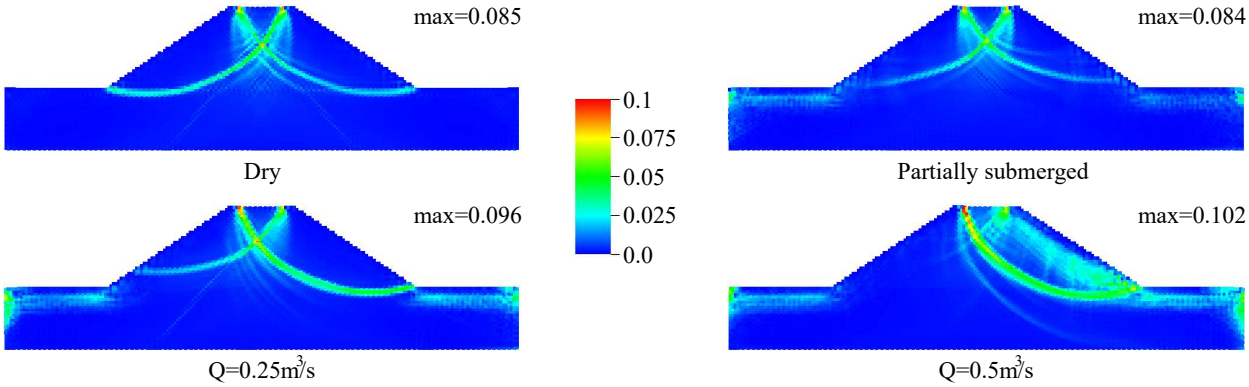

Figure 14: Equivalent strain distributions at the plate displacement of 6cm for all scenarios

With further loading and penetration of the loading plate into the crest of the embankment, the post-failure evolution and deformation can be studied. The shear deformation naturally increased with further loading showing a more concentrated picture of shear planes (Fig. 15a). Under the submerged condition of scenario (4), these shear planes still being symmetric seem to be diffused at the transition from the embankment to the foundation which is surprising as this cannot be recognised at the fully dry condition. For scenario (2) and (3), the flowing water forced the development of a shear plane toward the downstream side toe of the slope. The shear zone clearly penetrates into the foundation and causes the largest deformation at the downstream side toe.

These observations are confirmed by the changes in the geometry of the embankment with further loading shown in Fig. 15b. Scenario (3) shows here the largest deformation at the downstream side toe. Furthermore, the comparison of the deformed shapes confirms that the deformation in the dry condition of scenario (1) is completely symmetric and happened mainly at the interface of the embankment to the foundation. In contrast, for the submerged situation of scenario (4) the toes of the embankment on both sides, up- and downstream, did not move at all. It rather seems that the main deformation happens in half the height of the embankment. In the case of scenario (3) with $Q = 0.5m^3/s$, the upstream side slope seems to remain intact while the downstream side slope shows the largest deformation. The deformed shape for the moderate

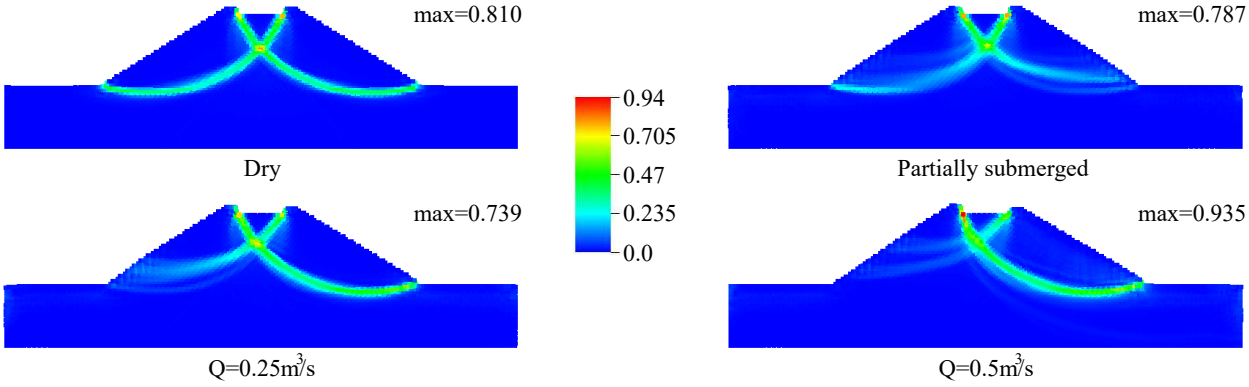

(a) Equivalent strain distributions at the plate displacement of $50cm$

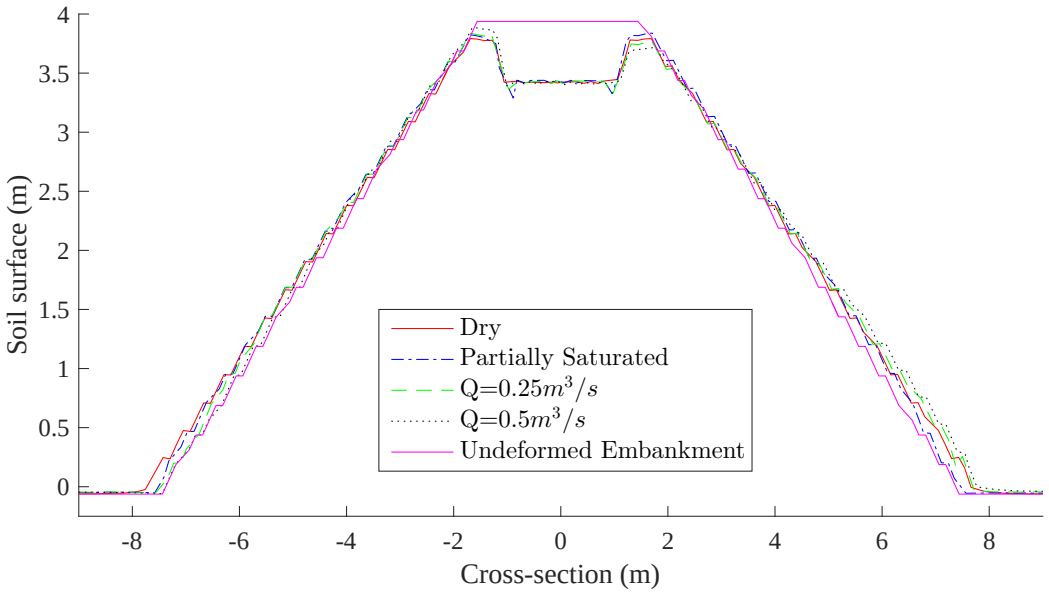

(b) Overall embankment shapes at the plate displacement of $50cm$

Figure 15: Post-failure behaviour for all scenarios

flood case of scenario (2) shows mixed deformation to both sides. In general, the failure mode in the dry and partially saturated cases show shear deformations leading to primarily vertical deformation while in the cases with flowing water shear failure in the form of sliding prevails. The insights into the deformation behaviour after large displacements of the loading plate and deformations of the embankment clearly show the advantages of an SPH approach enabling numerical simulations of large deformation.

5. Conclusions

A two-phase SPH scheme for the simulation of hydro-mechanically coupled processes in soils is presented. The features of the presented scheme introduced for this study are:

- a new approach for determination of the effective stress is implemented through the submerged unit weight of soil,

- porous media seepage is either described by the Darcy's Law or the Forchheimer equation to be able to cover most common flow conditions in soils, and
- the empirical formulation of Den Adel [11] for representing partly turbulent flow conditions was calibrated.

Each implementation step of the presented scheme is accompanied by verification analysis using problems for which analytical or experimental solutions are available. These features provide the opportunity to overcome the issues addressed in the introduction, which is the overestimation of the pore water pressure in available schemes, alongside with considering water flow and water table changes during simulations. Furthermore, the provided approach is beneficial to avoid undesirable impacts of the known WCSPH pressure fluctuations in the estimation of the effective stress.

The capabilities of this numerical tool are demonstrated based on the study of the deformation behaviour of an embankment due to the simultaneous loading through overburden pressure and seepage flow. Three fundamentally very different scenarios are considered as four categories in this study: dry condition (no flood and no rain), flood with moderate intensity (lower seepage), severe flood (higher seepage), and partly submerged condition. Force-displacement curves, failure planes, and post-failure behaviours are comprehensively discussed for all considered scenarios. It was observed that the seepage flow changes the failure mode of the embankment from a purely plastic settlement to a progressive shear failure (sliding). In the scenario considering the partly submerged embankment, failure planes are initially indistinct and appear to be shallow which becomes visible by local expansion of the embankment. In contrast, in all other cases the failure planes passed through the foundation representing deeper failure planes. The results of the force-displacement curves in the cases of the flooding scenarios are characterised by fluctuations which are most probably caused by the local failure due to water flowing out of the seepage face at the downstream slope representing a rather gradual progression of the failure.

The results of the embankment study show clearly that the presented SPH scheme with suggested interaction approach is capable of simulating the basic interaction between hydraulic condition and mechanical consequences in hydraulically loaded earthen structures. The possibility of simulating the hydraulic and mechanical processes in such structures beyond the failure including large plastic deformations offers new possibilities in the design of many geotechnical structures. The developed code is open-source and available as PersianSPH[2].

It is noteworthy to mention that the presented model can cover a reasonably large permeability range with the introduction of Darcys law and the Forchheimer equation. However, this model is computationally expensive for low permeable soils, such as silt and clay, since the seepage process is significantly slower in these soils except for thin layers with high gradients.

Acknowledgement

The presented research is funded by the Australian Research Council Discovery Project, Hydraulic Erosion of Granular Structures: Experiments and Computational Simulations (DP120102188). The second author would like to acknowledge the support from the Advance Queensland Fellowship program (Grant number AQ-15188).

References

[1] S. Adami, X. Y. Hu, and N. A. Adams. A generalized wall boundary condition for smoothed particle hydrodynamics. *Journal of Computational Physics*, 231(21):7057–7075, 2012.

[2] M. Antuono, A. Colagrossi, S. Marrone, and D. Molteni. Free-surface flows solved by means of sph schemes with numerical diffusive terms. *Computer Physics Communications*, 181(3):532 – 549, 2010. ISSN 0010-4655. doi: http://dx.doi.org/10.1016/j.cpc.2009.11.002.

[2] http://korzani.wixsite.com/persiansph

[3] D. Beeman. Some multistep methods for use in molecular dynamics calculations. *Journal of computational Physics*, 20 (2):130–139, 1976.
[4] W. Benz and E. Asphaug. Simulations of brittle solids using smooth particle hydrodynamics. *Computer physics communications*, 87(1):253–265, 1995.
[5] H. H. Bui and R. Fukagawa. An improved sph method for saturated soils and its application to investigate the mechanisms of embankment failure: Case of hydrostatic pore-water pressure. *International Journal for Numerical and Analytical Methods in Geomechanics*, 37(1):31–50, 2013.
[6] H. H. Bui, K. Sako, and R. Fukagawa. Numerical simulation of soilwater interaction using smoothed particle hydrodynamics (sph) method. *Journal of Terramechanics*, 44(5):339–346, 2007.
[7] H. H. Bui, R. Fukagawa, K. Sako, and S. Ohno. Lagrangian meshfree particles method (sph) for large deformation and failure flows of geomaterial using elastic-plastic soil constitutive model. *International Journal for Numerical and Analytical Methods in Geomechanics*, 32(12):1537, 2008.
[8] H. H. Bui, K. Sako, R. Fukagawa, and J. Wells. Sph-based numerical simulations for large deformation of geomaterial considering soil-structure interaction. In *The 12th International Conference of International Association for Computer Methods and Advances in Geomechanics (IACMAG)*, volume 1, pages 570–578. Citeseer, 2008.
[9] W. F. Chen and E. Mizuno. *Nonlinear analysis in soil mechanics*. Elsevier Amsterdam, 1990.
[10] R. A. Dalrymple and O. Knio. Sph modelling of water waves. In H. Hanson and M. Larson, editors, *Coastal Dynamics*. ASCE, 2001.
[11] H. Den Adel. Analysis of permeability measurements using forchheimers equation. Technical report, TU Delft, 1986.
[12] A. Fakhimi and M. Lanari. Demsph simulation of rock blasting. *Computers and Geotechnics*, 55:158 – 164, 2014.
[13] I. Federico, S. Marrone, A. Colagrossi, F. Aristodemo, and M. Antuono. Simulating 2d open-channel flows through an sph model. *European Journal of Mechanics - B/Fluids*, 34(0):35–46, 2012.
[14] S. Galindo-Torres, D. Pedroso, D. Williams, and H. Mühlhaus. Strength of non-spherical particles with anisotropic geometries under triaxial and shearing loading configurations. *Granular Matter*, 15(5):531–542, 2013.
[15] S. Galindo-Torres, A. Scheuermann, H. Mühlhaus, and D. Williams. A micro-mechanical approach for the study of contact erosion. *Acta Geotechnica*, 10(3):357–368, 2015.
[16] M. Gholami Korzani, S. A. Galindo-Torres, D. Williams, and A. Scheuermann. Numerical simulation of tank discharge using smoothed particle hydrodynamics. *Applied Mechanics and Materials*, 553:168–173, 2014. ISSN 3038350680. doi: 10.4028/www.scientific.net/AMM.553.168.
[17] M. Gholami Korzani, S. Galindo Torres, A. Scheuermann, and D. J. Williams. Smoothed particle hydrodynamics into the fluid dynamics of classical problems. *Applied Mechanics and Materials*, 846:73–78, 2016. ISSN 3038355283. doi: 10.4028/www.scientific.net/AMM.846.73.
[18] M. Gholami Korzani, S. A. Galindo-Torres, A. Scheuermann, and D. Williams. Parametric study on smoothed particle hydrodynamics for accurate determination of drag coefficient for a circular cylinder. *Water Science and Engineering*, 2017. ISSN 1674-2370. doi: http://dx.doi.org/10.1016/j.wse.2017.06.001.
[19] R. A. Gingold and J. J. Monaghan. Smoothed particle hydrodynamics: theory and application to non-spherical stars. *Monthly notices of the royal astronomical society*, 181(3):375–389, 1977.
[20] J. Grabe and B. Stefanova. Numerical modeling of saturated soils, based on smoothed particle hydrodynamics (sph). *geotechnik*, 37(3):191–197, 2014.
[21] J. Grabe and B. Stefanova. Numerical modeling of saturated soils based on smoothed particle hydrodynamics (sph). *geotechnik*, 38(3):218–229, 2015.
[22] J. P. Gray, J. J. Monaghan, and R. P. Swift. Sph elastic dynamics. *Computer methods in applied mechanics and engineering*, 190(49):6641–6662, 2001.
[23] R. W. Hockney and J. W. Eastwood. *Computer simulation using particles*. Adam Hilger, Bristol and New York, 1989.
[24] Y. Huang, W. Zhang, Z. Dai, and Q. Xu. Numerical simulation of flow processes in liquefied soils using a soil–water-coupled smoothed particle hydrodynamics method. *Natural Hazards*, 69(1):809–827, 2013. doi: 10.1007/s11069-013-0736-5. URL `http://dx.doi.org/10.1007/s11069-013-0736-5`.
[25] A. Koelewijn and H. Lottum. Full-scale field validation of innovative dike monitoring systems. 18th int. In *Conference on Soil Mechanics and Geotechnical Engineering*, pages 931–934, 2013.
[26] T. W. Lambe and R. V. Whitman. *Soil mechanics*. Wiley, New York, 1969.
[27] A. Larese, R. Rossi, E. Onate, and S. Idelsohn. A coupled pfem–eulerian approach for the solution of porous fsi problems. *Computational mechanics*, 50(6):805–819, 2012.
[28] A. Larese, R. Rossi, E. Oñate, M. Á. Toledo, R. Morán, and H. Campos. Numerical and experimental study of overtopping and failure of rockfill dams. *International Journal of Geomechanics*, 15(4):04014060, 2013.
[29] J. C. Lattanzio, J. J. Monaghan, H. Pongracic, and M. P. Schwarz. Controlling penetration. *SIAM Journal on Scientific and Statistical Computing*, 7(2):591–598, 1986.
[30] S. Li and W. K. Liu. *Meshfree particle methods*. Springer, Berlin ; New York, 2004.
[31] G. R. Liu and M. B. Liu. *Smoothed particle hydrodynamics : a meshfree particle method*. World Scientific, New Jersey, 2005.
[32] M. Liu and G. Liu. Smoothed particle hydrodynamics (sph): an overview and recent developments. *Archives of computational methods in engineering*, 17(1):25–76, 2010.
[33] L. B. Lucy. A numerical approach to the testing of the fission hypothesis. *The astronomical journal*, 82:1013–1024, 1977.
[34] N. Melnikova, G. Shirshov, and V. Krzhizhanovskaya. Virtual dike: multiscale simulation of dike stability. In *Proceedings of the International Conference on Computational Science (ICCS)*, volume 4, pages 791 – 800, 2011.
[35] J. J. Monaghan. Particle methods for hydrodynamics. *Computer Physics Reports*, 3(2):71–124, 1985.

[36] J. J. Monaghan. An introduction to sph. *Computer Physics Communications*, 48(1):89–96, 1988.
[37] J. J. Monaghan. Simulating free surface flows with sph. *Journal of computational physics*, 110(2):399–406, 1994.
[38] J. J. Monaghan. Smoothed particle hydrodynamics. *Reports on progress in physics*, 68(8):1703, 2005.
[39] J. J. Monaghan. Smoothed particle hydrodynamic simulations of shear flow. *Monthly Notices of the Royal Astronomical Society*, 365(1):199–213, 2006.
[40] J. J. Monaghan and R. A. Gingold. Shock simulation by the particle method sph. *Journal of computational physics*, 52 (2):374–389, 1983.
[41] J. J. Monaghan and H. Pongracic. Artificial viscosity for particle methods. *Applied Numerical Mathematics*, 1(3):187–194, 1985.
[42] J. P. Morris, P. J. Fox, and Y. Zhu. Modeling low reynolds number incompressible flows using sph. *Journal of computational physics*, 136(1):214–226, 1997.
[43] A. Panizzo. *Physical and Numerical Modelling of Subaerial Landslide Generated Waves*. Phd thesis, Universita degli Studi di L'Aquila, 2004.
[44] S. Shao and E. Y. M. Lo. Incompressible sph method for simulating newtonian and non-newtonian flows with a free surface. *Advances in Water Resources*, 26(7):787–800, 2003.
[45] J. Swegle, S. Attaway, M. Heinstein, F. Mello, and D. Hicks. An analysis of smoothed particle hydrodynamics. Technical report, Sandia National Labs., Albuquerque, NM (United States), 1994.
[46] M. R. A. Van Gent. Stationary and oscillatory flow through coarse porous media. Technical report, TU Delft, 1993.
[47] C. Wang, Y. Wang, C. Peng, and X. Meng. Smoothed particle hydrodynamics simulation of water-soil mixture flows. *Journal of Hydraulic Engineering*, 142(10):04016032, 2016.
[48] C. Zwanenburg, E. Den Haan, G. Kruse, and A. Koelewijn. Failure of a trial embankment on peat in booneschans, the netherlands. *Géotechnique*, 62(6):479–490, 2012.